Improved Bathymetric Prediction using Geological Information: SYNBATH

David T. Sandwell[1], John A. Goff[2], Julie Gevorgian[1], Hugh Harper[1], Seung-Sep Kim[3], Yao Yu[1], Brook Tozer[4], Paul Wessel[5], and Walter H. F. Smith[6]

[1]Scripps Institution of Oceanography, University of California San Diego, La Jolla, CA, USA
[2]Institute for Geophysics, Jackson School of Geosciences, University of Texas at Austin, Austin, TX, USA
[3]Department of Geological Sciences, Chungnam National University, Daejeon, Korea
[4]GNS Science, Wellington, New Zealand
[5]Department of Earth Sciences, SOEST, University of Hawaii at Manoa, Honolulu, Hawaii, USA
[6]Laboratory for Satellite Altimetry, NOAA, College Park, MD, USA

Submitted to: Earth and Space Science, October 8, 2021

Key Points

- Approximately 20% of the ocean floor topography has been surveyed by ships, the remaining 80% is predicted by satellite altimetry.
- We increased the resolution of the predicted depth using spectral properties of abyssal hills and the characteristic shapes of seamounts.
- We estimate the height and radius of 19,000 uncharted seamounts.

Abstract

To date, approximately 20% of the ocean floor has been surveyed by ships at a spatial resolution of 400 m or better. The remaining 80% has depth predicted from satellite altimeter-derived gravity measurements at a relatively low resolution. There are many remote ocean areas in the southern hemisphere that will not be completely mapped at 400 m resolution during this decade. This study is focused on the development of synthetic bathymetry to fill the gaps. There are two types of seafloor features that are not typically well resolved by satellite gravity: abyssal hills and small seamounts (< 2.5 km tall). We generate synthetic realizations of abyssal hills by combining the measured

statistical properties of mapped abyssal hills with regional geology including fossil spreading rate/orientation, rms height from satellite gravity, and sediment thickness. With recent improvements in accuracy and resolution, It is now possible to detect all seamounts taller than about 800 m in satellite-derived gravity and their location can be determined to an accuracy of better than 1 km. However, the width of the gravity anomaly is much greater than the actual width of the seamount so the seamount predicted from gravity will underestimate the true seamount height and overestimate its base dimension. In this study we use the amplitude of the vertical gravity gradient (VGG) to estimate the mass of the seamount and then use their characteristic shape, based on well surveyed seamounts, to replace the smooth predicted seamount with a seamount having a more realistic shape.

Keywords: global bathymetry, uncharted seamounts, abyssal hills

Introduction

Bathymetry is foundational data, providing basic infrastructure for scientific, economic, educational, military, and political work. High resolution, deep ocean bathymetry is critical for: (1) understanding the geologic processes responsible for creating ocean floor features unexplained by simple plate tectonics, such as abyssal hills, seamounts, microplates, propagating rifts, and intraplate deformation; (2) determining the effects of bathymetry and seafloor roughness on ocean circulation, ocean mixing, and climate; and (3) understanding how marine life is influenced by seafloor depth, roughness, and interactions of currents with the seafloor [*Yesson et al.,* 2011]. The Seabed 2030 project [https://seabed2030.org] "aims to bring together all available bathymetric data to produce the definitive map of the world ocean floor by 2030 and make it available to all." The Seabed 2030 global compilation will be based on swath mapping using multibeam sonar which has a spatial resolution of about 400 m at a typical ocean depth of 4 km [*Mayer et al.,* 2018].

The Seabed 2030 project has made considerable progress over the past few years by increasing the multibeam coverage in public compilations from 11% [e.g., GEBCO 2019; Tozer et al., 2019] to more than 20% today [GEBCO 2021]. Much of this data has been made available by the international community with nearly complete coverage of several exclusive economic zones as well as dense coverage of areas of high scientific interest. The remaining 80% of the seafloor has depth predicted from a combination of spatially dense satellite altimeter gravity measurements and sparse soundings to provide the large-scale shape of the ocean basins as well as to calibrate the local ratio of bathymetry-to-gravity [e.g., *Smith and Sandwell,* 1994]. The spatial resolution of these predicted depths is limited to approximately the mean ocean depth because of the upward continuation smoothing effects from Newton's law of gravity. The best satellite gravity models available today can only resolve ½ wavelength of 6 km when the regional depth is 4 km [*Tozer et al.*, 2019]. Thus, the resolution of gravity-predicted depth is more than 10 times worse than the Seabed 2030 objective.

There are many remote ocean areas in the southern hemisphere that will probably not be completely mapped at 400 m resolution during this decade and well beyond (e.g., Figure 1). This study is focused on the development of **SYNthetic BATHymetry (SYNBATH)** to fill the gaps. The synthetic bathymetry has the geostatistical properties of real seafloor bathymetry but it is not as accurate as ship soundings. While the synthetic data will be replaced with real soundings as they become available in the future, in the interim such realistic realizations can provide key inputs for a number of important scientific applications. We will discuss such applications, where this synthetic bathymetry is appropriate and valuable, and also discuss uses of synthetic bathymetry that could prove problematic and result in a false impression that Seabed 2030 objectives have been achieved.

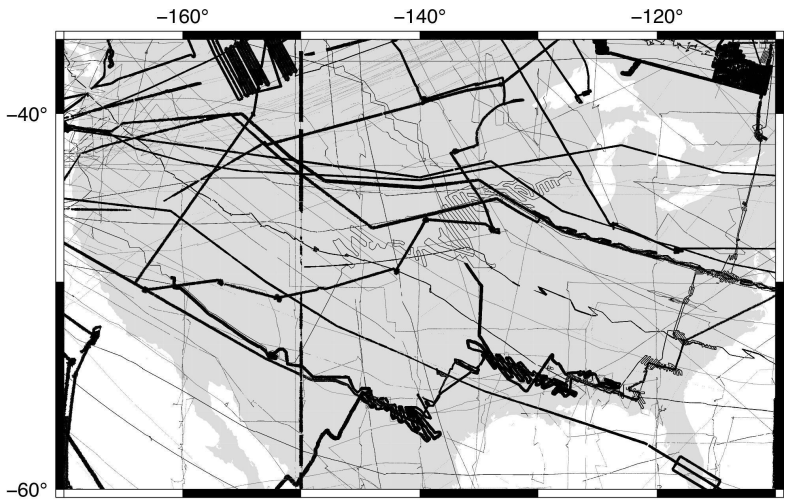

Figure 1. Available ship soundings including single- and multi-beam data in a remote region of the South Pacific based on the GEBCO 2021 bathymetry [*Weatherall et al.,* 2020] grid superimposed on a map of North America for scale. There are many areas on this map that are more than 100 km from a depth sounding. Moreover, removal of the lower resolution single beam soundings would dramatically reduce the spatial coverage leaving many gaps greater than 400 km.

There are two types of seafloor features that are not well resolved by satellite gravity. These are abyssal hills and small seamounts (< 2.5 km tall). As described more completely in the next section, one can generate synthetic abyssal hills by combining the measured statistical properties of mapped abyssal hills with regional geology including fossil spreading rate/orientation, rms height from satellite gravity, and sediment thickness [*Goff and Arbic*, 2010; *Goff*, 2020]. At scales greater than about 6 km ½ wavelength, the location or "phase" of the synthetic hills matches the actual location based on gravity predicted depth. At shorter scales, the synthetic hills have the correct power spectral roll-off and orientation but have random locations completely uncorrelated with the actual abyssal hills. For studies in physical oceanography, creating hills with the correct height, spectral slope and orientation is more important than hills having the correct location or phase.

The second type of unresolved seafloor feature are seamounts less than about 2.5 km tall [*Menard,* 1964; *Staudigel et al.,* 2010; *Kim and Wessel,* 2011; 2015]. Because of significant improvements in the accuracy and resolution of the satellite gravity since the

Kim and Wessel [2011] study, it is now possible to detect seamounts taller than about 800 m [*Gevorgian et al.,* 2021] and their location can be determined to an accuracy of better than 1 km. However, the width of the gravity bump is much greater than the actual width of the seamount. Therefore, the seamount predicted from gravity will underestimate the seamount height and overestimate its base dimension. This results in a seamount flank slope that may be 10 times smaller than the actual slope [*Becker and Sandwell*, 2008]. As in the case of abyssal hills, the magnitude of the slope of the seamount influences the paths of currents as well as the generation of eddies and internal waves. The studies by *Smith* [1988] and *Gevorgian et al.,* [2021] have used depth soundings to characterize the shapes of smaller seamounts. In this study we use the amplitude of the vertical gravity gradient (VGG) to estimate the mass of the seamount and then use their characteristic shape to replace the smooth predicted seamount with a Gaussian seamount having a more realistic shape.

Modeling Abyssal Hills

We use the model of *Goff and Jordan* [1988; 1989] to generate synthetic abyssal hills; the power spectrum of the topography has the following functional form

$$P\left(k_x,k_y\right)=\frac{\pi h_{rms}^2}{\nu k_n k_s}\left[\frac{k_h^2}{k_s^2}\cos^2\left(\theta-\theta_s\right)+\frac{k_h^2}{k_n^2}\sin^2\left(\theta-\theta_s\right)\right]^{-(\nu+1)} \quad (1)$$

where $\left(k_x,k_y\right)$ is the 2-D wavenumber, $k_h=\left(k_x^2+k_y^2\right)^{1/2}$ is the magnitude of the 2-D wavenumber, h_{rms} is the rms of the abyssal hill height, $\left(k_s,k_n\right)$ are the characteristic wavenumbers for the abyssal hills in the strike and normal directions, respectively, θ_s is the azimuth of the strike of the abyssal hills and ν is the Hurst number (~0.9) that

140 determines the rate of spectral roll-off. The five parameters $(h_{rms}, k_s, k_n, \theta_s, \nu)$ vary
141 geographically depending on the geological setting at the time of the formation of the
142 abyssal hills [*Goff,* 2020]. In addition, as the plate ages, sediments can partially or fully
143 cover the hills which reduces their visible height.
144
145 The rms height h_{rms} of the hills is taken from the most recent analysis [*Goff,* 2020] of the
146 altimeter-derived gravity anomaly [*Sandwell et al.,* 2019]. RMS height was reduced in
147 sediment covered areas by a factor of 0.1 times the sediment thickness [*Straume et al.,*
148 2019]. The characteristic wavenumbers (k_s, k_n) and Hurst number ν were taken from
149 the analysis of *Goff* [2010] and the orientation of the abyssal hills θ_s is from the recent
150 global age compilation of *Seton et al.* [2020].
151
152 To replace the predicted bathymetry with more realistic abyssal fabric, we first prepare
153 the 5 global parameter grids (+/- 74 degrees latitude) to have consistent spatial
154 coverage. This was done by extending the grids of $(k_s, k_n, \theta_s, \nu)$ and then tapering the
155 rms height grid h_{rms} to go smoothly to zero on its perimeter. As in the previous studies
156 [e.g., *Goff and Arbic*, 2010], we populate a 30 arcsecond global grid with uniform
157 random cell values. A 2-D spatial filter is calculated from the inverse transform of the
158 spectral model in equation 1 at each cell location and convolved with the random grid; a
159 new filter is computed at each grid cell to accommodate the spatial variations in the 5
160 parameters. This operation is equivalent to inverse Fourier transformation of the
161 product of the amplitude spectrum with a random phase spectrum. However, though
162 computationally far more efficient, this alternative does not allow for the imposition of
163 the statistical heterogeneity that is critical for our purposes. The resulting synthetic
164 bathymetry (e.g., Figure 2) is added to a previous iteration of global depth to make a
165 new synthetic bathymetry data set. We then perturb the global predicted bathymetry
166 model to exactly match these synthetic data using a standard remove/grid/restore
167 approach. A spline in tension gridder is used [*Smith and Wessel,* 1990]. This becomes an

updated predicted depth that is used in a second remove/grid/restore using the real sounding data. The final result exactly matches the real soundings where they exist and blends smoothly into the updated predicted depth in the data voids. The fully sedimented areas and areas with no abyssal hill predictions have depth based entirely on sparse soundings and the gravity prediction.

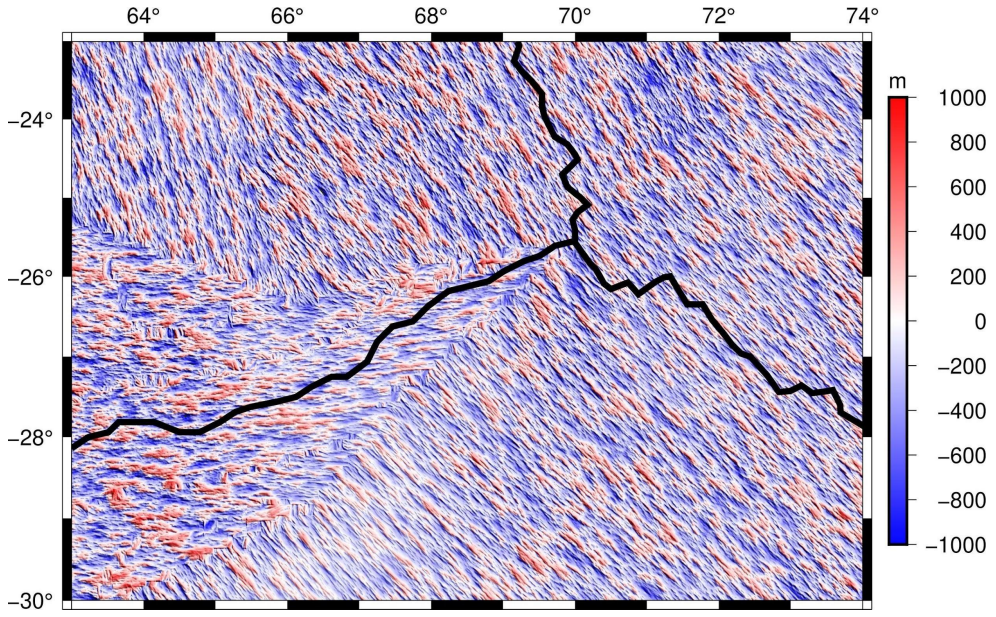

Figure 2. Example of synthetic abyssal hills around the Indian Ocean Triple Junction illustrate their variation with spreading direction and rate.

Mapping Seamounts

Although multibeam sonar is best suited for mapping smaller seamounts, satellite altimetry can be used to find larger seamounts (> 700 m) through disturbances in Earth's gravity field. These perturbations are due to the difference in density between basalt and seawater. There are four main errors and uncertainties that arise from satellite altimetry: upward continuation, measurement noise, seafloor roughness, and sediment cover [*Wessel et al*., 2010]. The first global seamount maps (8556 seamounts) were created from widely-spaced Seasat altimeter profiles [*Craig and Sandwell*, 1988]. Since the Seasat mission there have been a number of altimeter missions that have greatly improved the accuracy and coverage of the gravity field [Wessel, 2001, 14639

seamounts]. This has enabled the construction of the vertical gravity gradient (VGG) which is a spatial derivative of the gravity field [e.g., *Wessel,* 1997]. This spatial derivative amplifies short wavelengths and suppresses long wavelengths so it is a valuable tool for locating smaller features on the ocean floor [*Kim and Wessel,* 2011; 2015]. However, the spatial derivative also amplifies short wavelength noise which limits seamount detectability. The recently released VGG has significantly lower noise levels because of new altimeter data from CryoSat-2, SARAL/AltiKa, Jason-1/2 and the Sentinel-3a/b missions [*Sandwell et al.,* 2014; 2019]. After comparing the old and new VGG, it was found that the signal to noise ratio has increased by at least a factor of 2, indicating that multiple altimetry sources can improve gravity data and help find unmapped features on the ocean floor.

Gevorgian et al., [2021] have used the latest version of the VGG model [*Sandwell et al.,* 2019] to update the global seamount catalog of *Kim and Wessel* [2011; 2015]. The original KW catalog had 24643 seamount identifications. The new analysis was performed in 4 steps using the display and digitization features in Google Earth: 1) The VGG was displayed as a grey-scale image with black-to-white saturation set at -53 to +38 Eotvos units. 2) Known tectonic features [*Matthews et al.,* 2011] were plotted as lines. 3) The KW15 catalog was also plotted as points. 4) *Gevorgian et al.,* [2021] visually identified circular anomalies in the VGG in the deep ocean (> ~500 m) away from known and well-mapped tectonic features. The lower noise level in the latest VGG grid enabled the identification of circular anomalies as small as 5 Eotvos which is about ½ the threshold of the KW15 analysis. *Gevorgian et al.,* [2021] found 10796 previously unidentified seamounts and also determined that 513 seamounts in the KW15 catalog were mis-identifications. The revised KW catalog has 24129 seamounts so the total seamount count is 34925. Figure 3 shows a region on the eastern flank of the East Pacific Rise where there is complete multibeam coverage. The VGG image shows numerous circular anomalies associated with small seamounts. We use these to develop a method of estimating seamount height and radius from the VGG anomaly.

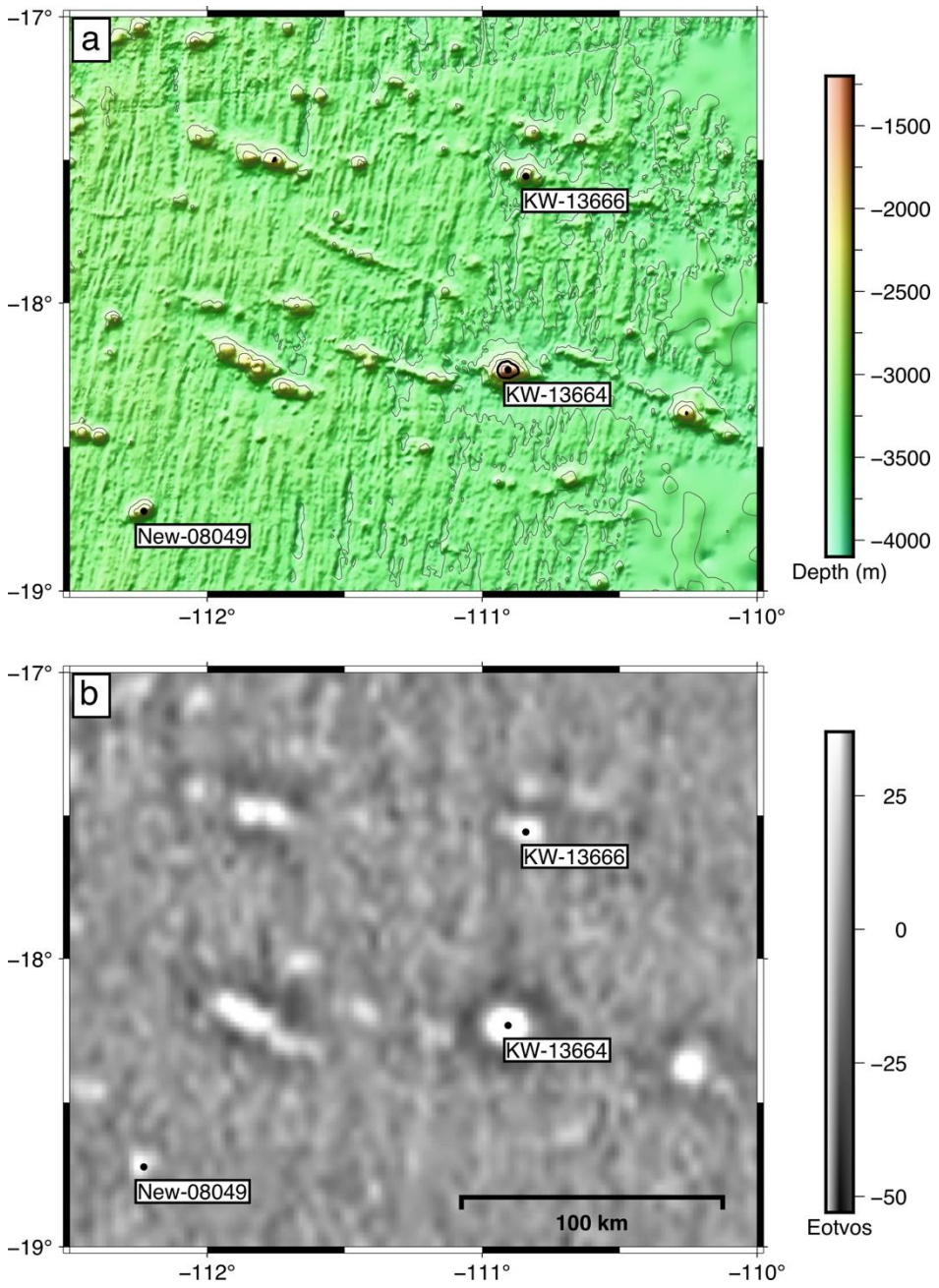

Figure 3. (a) Bathymetry on the eastern side of the East Pacific Rise (EPR) where three seamounts have been mapped by multibeam sonar. The two labeled KW are from the Kim and Wessel [2011] catalog while the seamount labelled New-08049 is from *Gevorgian et al.,* [2021]. (b) VGG in the same area showing three seamounts that are relatively circular.

Modeling Seamounts

Previous studies have found that small seamounts are typically circular in planform and have a fixed height to base ratio largely independent of height [*Smith and Jordan,* 1988;

Wessel, 2001]. *Smith* [1988] studied bathymetry profiles across 85 seamounts and found they could be fit by a flattened cone having a height to base radius ratio of ~0.21 and a flattening of 0.15. More recently, *Gevorgian et al.,* [2021] studied 739 seamounts having good bathymetry coverage and found they are best fit by a Gaussian function

$$h(r) = h_o e^{\frac{-r^2}{2\sigma^2}} \quad (2)$$

where h_o is the seamount height, r is the radius from the center of the seamount, and σ is the characteristic width of the seamount. Their analysis found a high correlation between seamount radius and slope such that that $\sigma = 2.4h_o$. This corresponds to a maximum seamount slope of 0.25 independent of seamount height. Here we use this model, along with the observed VGG, to estimate the shape of each seamount. There are several parameters that go into this gravity modeling including mean ocean depth surrounding the seamount d_o, seamount density relative to seawater $\Delta\rho$, crustal thickness, elastic thickness, mantle density, and seamount height h_o. We show next that for seamounts < ~2 km in height, the VGG is insensitive to the elastic thickness so we can assume the seamounts are uncompensated. In this case the mean crustal thickness and mantle density are not needed.

This insensitivity to elastic thickness is easily verified using the *grdseamount* and *gravfft* modules in Generic Mapping Tools (GMT) [*Wessel et al.,* 2019]. A typical seamount, shown in Figure 4, has a height of 1500 m, a $\sigma = 2.4h_o$, a density of 2700 kg m^{-3}, and a base depth of 4000 m. To assess the effects of elastic thickness, we computed the VGG, including 3 nonlinear terms in the *Parker* [1973] expansion. For an elastic thickness Te of 2 km as well as 100 km (uncompensated), the two VGG models have almost equal signatures so we can assume small seamounts are uncompensated as in [*Watts et al.* 2006].

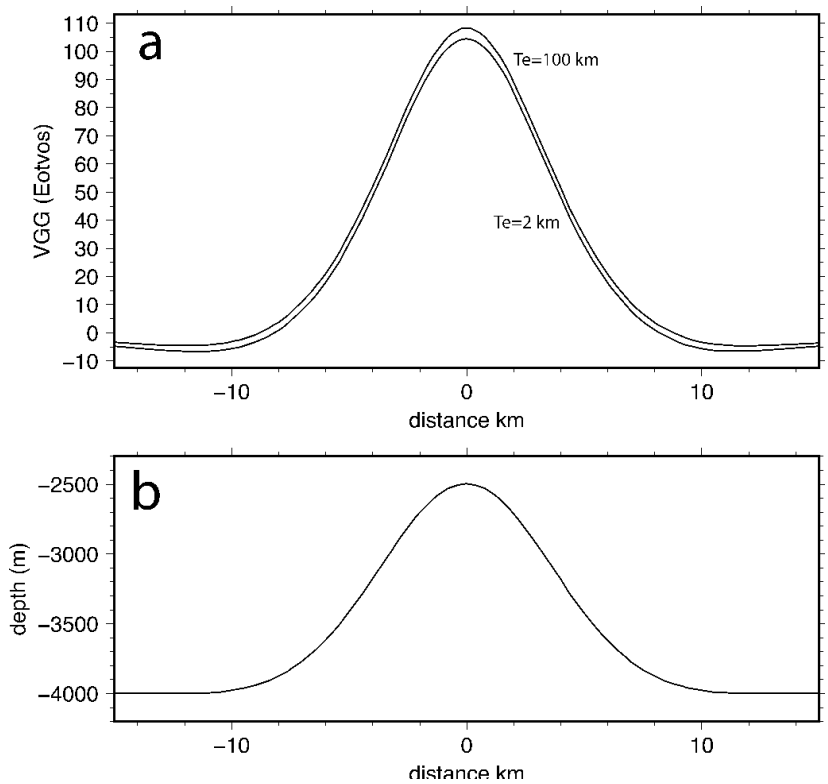

Figure 4. Vertical gravity gradient (VGG - a) computed from a Gaussian seamount (b) that is 1500 m tall, has a $\sigma = 2.4h_o$. The two VGG curves, which are very similar, correspond to well compensated topography (Te = 2 km) and uncompensated topography (Te = 100 km).

Based on this calculation the remaining free parameters are seamount height, seamount density, and base depth. The base depth is calculated from the median depth in a 90 km by 90 km area surrounding the seamount to be modelled.

To further test the validity of this simple model for a small seamount we analyzed topography and VGG for three seamounts in an area of the southern East Pacific Rise where there is complete multibeam coverage (Figure 3). Two of the seamounts are from the *Kim and Wessel* [2011] compilation while the third is recently identified in the VGG [*Gevorgian et al.,* 2021]. The basic characteristics of the seamounts are provided in Table 1.

Table 1. Characteristics of modeled seamounts

label	lon	lat	base depth(m)	seamount height (m)	gravity (mGal)	VGG (Eotvos)
KW-13664	-110.90	-18.23	3461.5	2140	53.4	143.7
KW-13666	-110.84	-17.54	3409.5	1343.5	18.5	50.8
New-08049	-112.23	-18.71	3255.5	1209.5	12.9	44.7

Using these well surveyed seamounts, we can perform forward modeling to establish the density that provides the best fit. From the observed topography we calculate the VGG and compare with the observations. An additional low-pass filter, with a wavelength of 16 km, was applied to the model VGG to match the low-pass filtering that was used to construct the VGG data [*Sandwell et al.,* 2019]. Table 2 shows the median absolute deviation (L1-norm) as a function of seamount/crustal density for each of the three seamounts. We find that the misfit is not very sensitive to the density. A much more extensive study by *Watts et al.* [2006] using 9752 seamounts shows the best density is 2800 kg m^{-3}. This value is consistent with our results from modeling just three small seamounts.

Table 2. Misfit (L1-norm) versus seamount density in Eotvos

	2650 kg m^{-3}	2700	2750	2800	2850	2900	no model
KW-13664	4.51	4.34	4.33	4.43	4.50	4.56	10.49
KW-13666	4.35	4.28	4.19	4.19	4.20	4.21	8.74
New-08049	4.49	4.51	4.53	4.54	4.54	4.45	5.51

An example of the fit of the model to the largest of the three seamounts is shown in Figure 5. The model based on topography with a density of 2800 kg m^{-3} provides an excellent fit to the VGG data. As a final check we generated VGG models using a Gaussian approximation to the actual seamount topography for large and small seamounts in the region. These results, shown in Figures 5 and 6, demonstrate that the VGG from a Gaussian seamount is a good match to the VGG from the actual seamount topography. The important parameter is the seamount height. Since most seamounts

297 are uncharted we will use this approach, with a Gaussian shaped seamount, to generate
298 synthetic seamounts in unmapped areas.

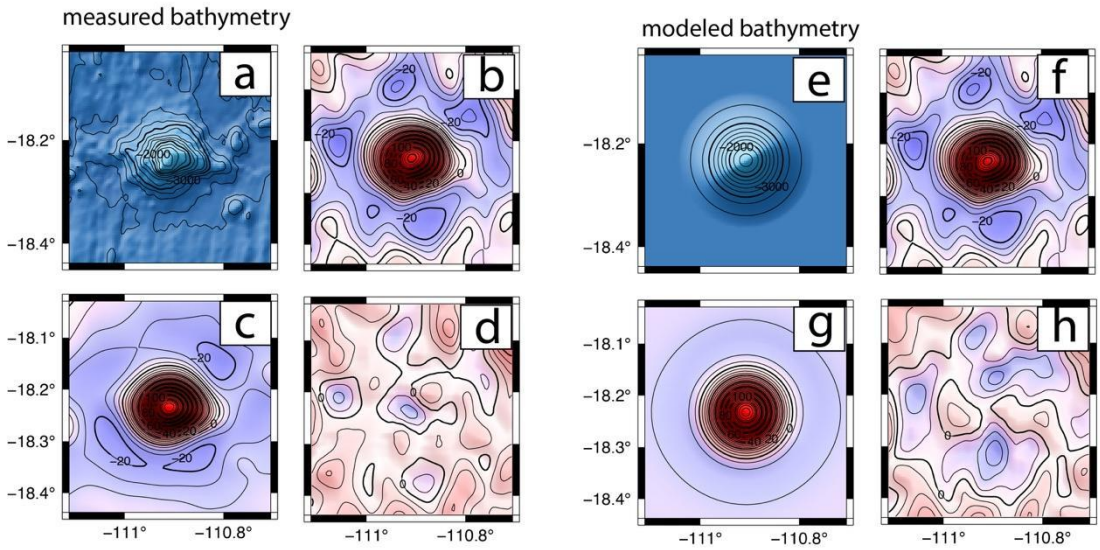

299
300 Figure 5. (a) Bathymetry of the largest of the three seamounts, KW-13664 (200 m contours). (b, f)
301 Measured VGG for seamount (5 Eotvos contours). (c) Model VGG using a density of 2800 kg m^{-3}. (d)
302 Difference between observed VGG and model VGG (L1 4.43 Eotvos, 5 Etovos contours). (e) Model
303 bathymetry using a Gaussian seamount (200 m contours). (g) Model VGG for Gaussian model bathymetry.
304 (h) Difference between observed VGG and Gaussian model VGG (L1 7.04 Eotvos, 5 Etovos contours).
305

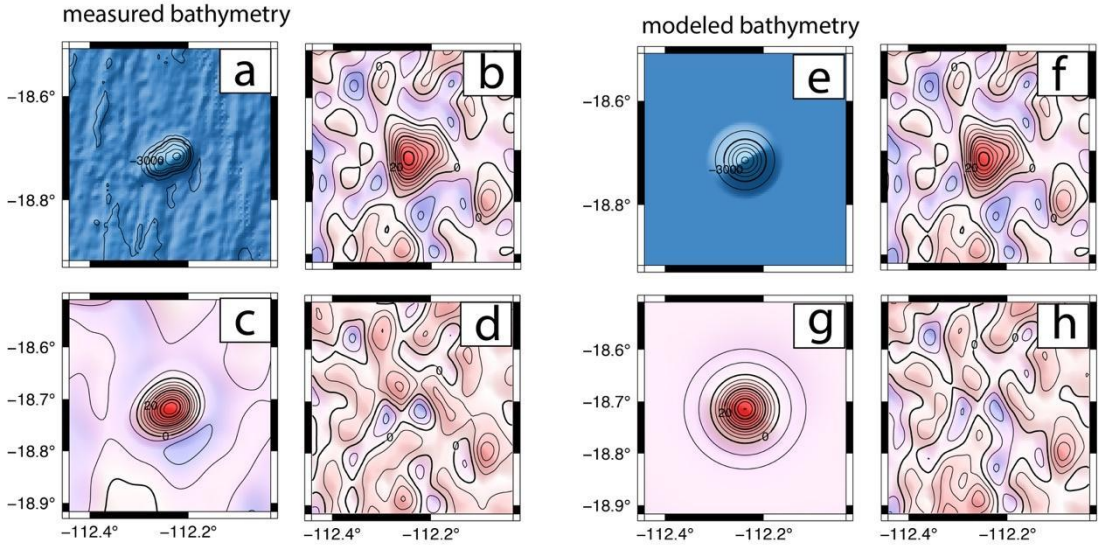

306
307 Figure 6. (a) Bathymetry of the smallest of the three seamounts, New-08049 (200 m contours). (b+f)
308 Measured VGG for seamount (5 Etovos contours). (c) Model VGG using a density of 2800 kg m^{-3}. (d)

Difference between observed VGG and model VGG (L1 4.54 Eotvos, 5 Etovos contours). (e) Model bathymetry using a Gaussian seamount. (g) Model VGG for Gaussian bathymetry (200 m contours). (h) Difference between observed VGG and conical model VGG (L1 5.13 Eotvos, 5 Etovos contours).

Based on this analysis, we estimated heights for 34925 seamounts in the updated catalog basically using the method of *Wessel,* [2001]. This was done by extracting a 90 km by 90 km grid of VGG and SRTM15 (V2.3) depth data centered on each seamount. The base depth was computed from the median depth and a Gaussian seamount (equation 2) was superimposed on this base depth using $\sigma = 2.4h_o$ a density of 2800 kg m^{-3}. The VGG model, generated using *gravfft* in GMT, was low-pass Gaussian filtered at 16 km wavelength to match the low-pass filter applied to the VGG data. Finally the L1 norm difference between the model and data VGG was computed for a 33 by 33 km area centered on the seamount. This modeling was repeated for seamount heights ranging from 700 to 2600 m in steps of 100 m. The model with the lowest misfit was selected as the height. A histogram of the number of seamounts versus their estimated height is shown in Figure 7 (top). A histogram of seamounts versus the L1 norm of the misfit is shown in Figure 7 (bottom). For all seamounts, the number increases with decreasing seamount height until 1300 m when the number decreases at smaller heights. Our results show that the KW analysis, using noisier VGG data, captured most seamounts taller than about 1500 m. The new analysis found many more seamounts with heights between 1100 and 1500 m. Most of the VGG models have misfits between 5 and ~20 Eotvos. The new seamounts are generally smaller and have lower L1-misfit. For the remainder of this study we exclude all seamounts with heights greater than 2500 m and less than 800 m since they are at the ends of the histogram. We also reduce the height of any seamount having a depth shallower than -100 m to force the model summit depth of -100 m. In other words we don't want to create any false islands or atolls although these cases may be interesting places to survey with multibeam. This results in 31602 modeled seamounts.

We investigate how many of these seamounts are constrained by depth soundings by using the SRTM15 V2.3 source identification grid (SID) to locate all the seamounts

having at least one sounding within 3 km of the center of the seamount. This resulted in 11879 seamounts that are at least partly constrained by a real depth sounding and 19723 seamounts that are completely uncharted.

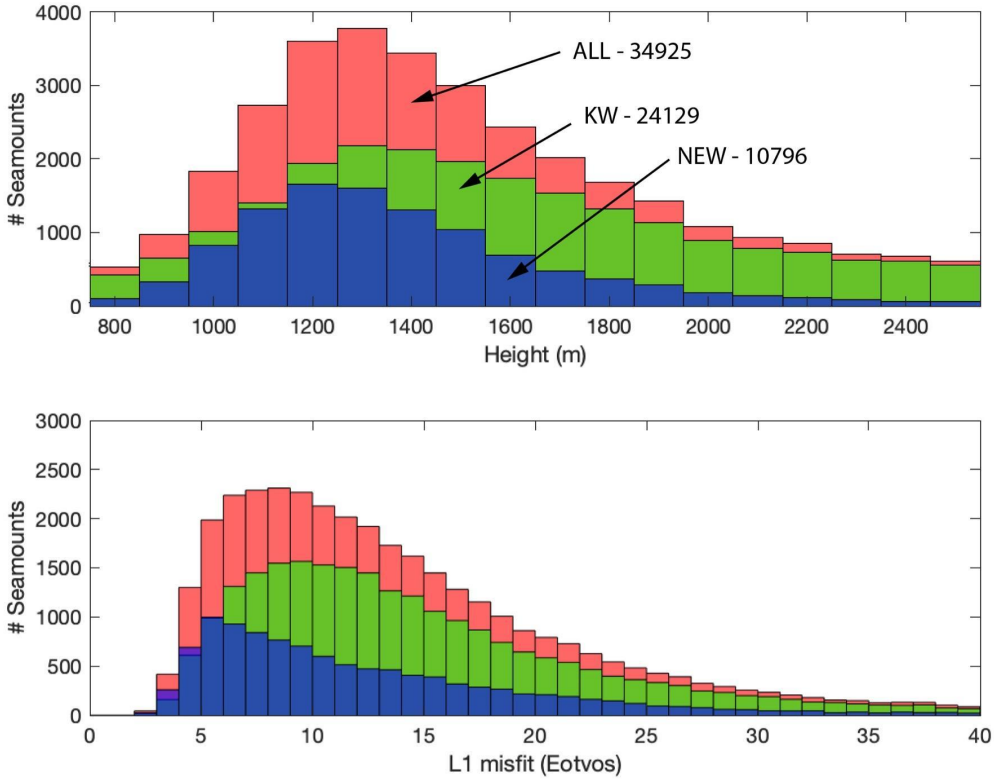

Figure 7 (top) Histogram of the seamount height based on our analysis of all seamounts (red), KW seamounts (green), and new seamounts (blue). (bottom) Histogram L1 misfit of model VGG to each seamount.

Results

Prior to filling the gaps with synthetic bathymetry, we assembled new sounding data not available for the *Tozer et al.,* [2019] study. The latest V2.3 of the SRTM15+ grid includes 905 new multibeam sonar cruises that are archived at the National Center for Environmental Information [https://www.ngdc.noaa.gov/mgg/bathymetry/multibeam.html]. These were processed with MB-System [*Caress and Chayes*, 2008] to remove outer beams and flatten the rails of the innermost beams, and subsequently used to update the 15-arcsecond grid. We performed 3 iterations of visual editing of bad soundings

(~700 edits) to prepare the grid as the base layer for the GEBCO 2022 global grid. In addition we obtained 9 large composite grids from IFREMER that greatly improved the bathymetry coverage of the Gulf of Aden [*Hebert et al.,* 2001], the Lesser Antilles volcanic arc [*Talbot and Loubrieu,* 2020], French Guiana margin [*Loubrieu,* 2019], the Rodrigues triple junction [*Mendel et al.,* 2000], the Kerguelen plateau [*Loubrieu,* 2019], Reunion island [*Sisvath et al.,* 2011], Saint-Paul and Amsterdam Islands [*Loubrieu et al.,* 2020], the Southwest Indian ridge [*Sauter and Mendel,* 2000], and the North Fiji basin [*Ruellan,* 2001].

Gaps in the SRTM15+ grid were filled with synthetic bathymetry to create SYNthetic BATHymetry (SYNBATH V1.2). An example of the enhancement related to just abyssal hills is shown in Figure 8. The upper plot shows the standard SRTM15+ grid with the combination of single- and multibeam bathymetry and smooth gravity-predicted depths filling the gaps. The Indian Ocean triple junction at 70˚ longitude and -25.7˚ latitude is the intersection of the Central Indian ridge (CIR) to the north, the Southeast Indian ridge (SEIR), and the Southwest Indian ridge (SWIR). The flanks of each ridge have ridge-parallel abyssal hills as seen in the available multibeam bathymetry. The slower spreading SWIR has left a V-shaped scar on the seafloor where there is a nearly 90˚ degree change in the orientation of the abyssal hills reflecting the change in age gradient [e.g., *Seton et al.*, 2020]. The center plot shows the SYNBATH bathymetry which is identical to the SRTM15+ bathymetry where there are real ship soundings and has synthetic abyssal hills in the gaps. The boundaries between the actual and synthetic bathymetry are difficult to observe. One would expect a sharp change in the “phase” of the abyssal hills across these boundaries. However, a part of the synthetic abyssal fabric contains a correct-phase pattern that is derived from the gravity prediction. Figure 8c shows the difference between the SYNBATH and SRTM15+ bathymetry grids. The difference is zero at grid cells constrained by ship data and matches the synthetic abyssal hills (Figure 2) in the gaps.

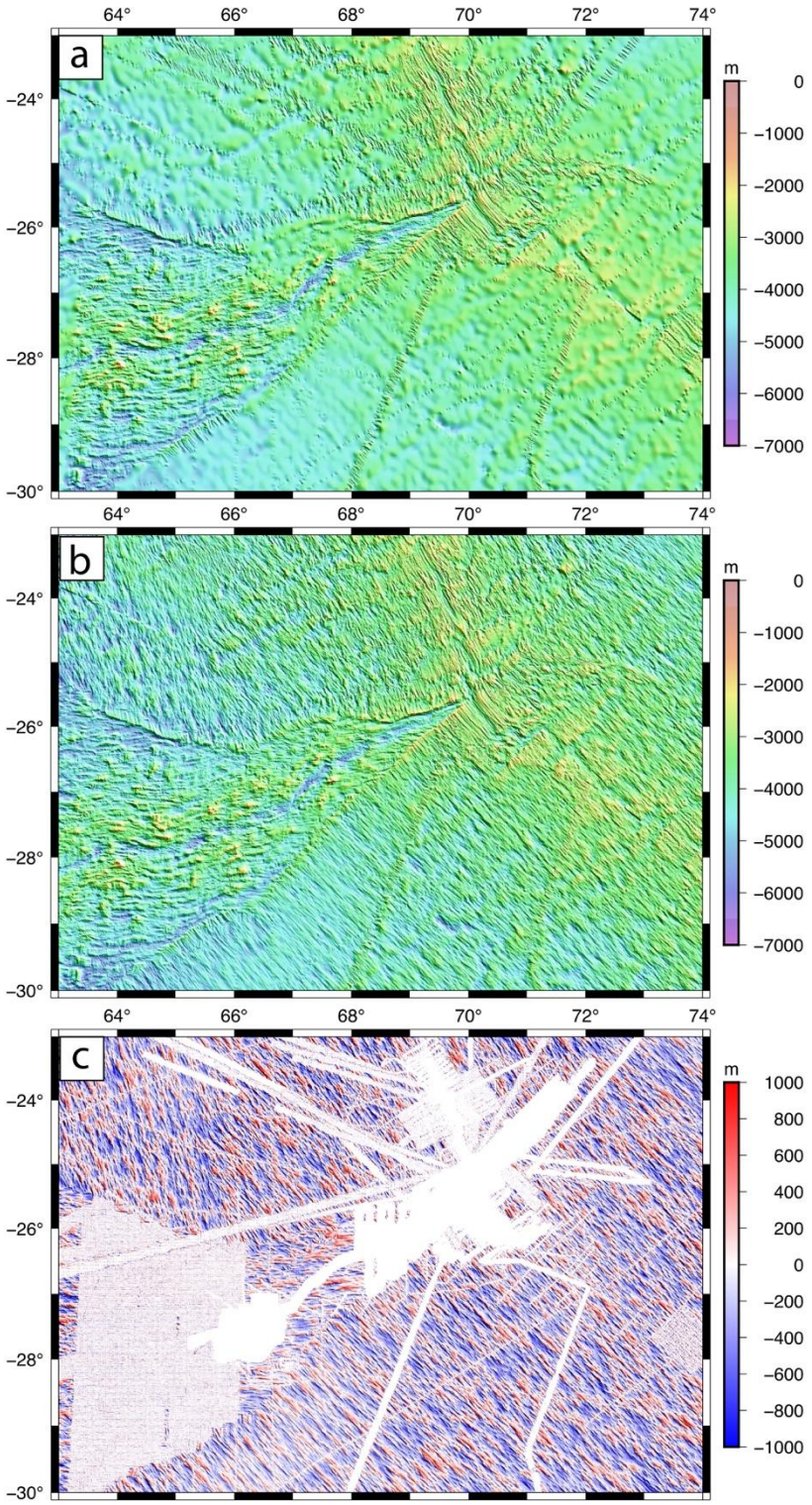

Figure 8. Bathymetry of Indian Ocean Triple Junction. (a) Based on multi- and single-beam soundings and gravity-predicted bathymetry to fill the gaps. (b) Based on multi- and single-beam soundings and synthetic abyssal hills superimposed on gravity-predicted bathymetry to fill the gaps. (c) Difference shows that the

391 two methods are identical where measured soundings are available and have synthetic abyssal hills in
392 other areas.
393
394 An example of the enhancement primarily related to small seamounts is shown in Figure
395 9 for a poorly charted region just south of the Galapagos spreading ridge. The smaller
396 predicted seamounts, having no bathymetry soundings, are short and wide (Figure 9a).
397 The sharpened seamounts are tall and narrow following the shape of the Gaussian
398 model $\sigma = 2.4h_o$ (Figure 9b). The difference between these two models (Figure 9c)
399 shows the combined effects of added abyssal fabric and sharpened seamounts. In areas
400 where there are actual multibeam depth soundings, the two models agree.
401
402 Since there are many steps in constructing this SYNBATH bathymetry at 15 arcseconds
403 we provide a brief overview. There is a common *polishing* technique used each time a
404 new data layer is added so we first describe that remove/grid/restore approach as
405 follows: 1) assemble some new data (e.g. real soundings or synthetic hills or seamounts;
406 2) remove the previous model from each new data point; 3) identify spatial gaps (> 20
407 km from a new data point) and add zero-valued data points at these locations; 4) use
408 the GMT *surface* module with a tension of 0.6 and a convergence limit of 1 m and up to
409 200 iterations; 5) add the previous model so the result exactly fits the new data. Given
410 this common *polishin*g approach the overall construction method is:
411
412 1) Use the gravity prediction method described in *Smith and Sandwell* [1994] and
413 updated in *Tozer et el.,* [2019] to make a global 1-minute bathymetry.
414 2) Polish that bathymetry using actual soundings.
415 3) Use the 1-minute base depth to generate synthetic abyssal hill data and
416 synthetic seamount data. So the model from step 2) provides the base depth for
417 both the hills and seamounts. Also note the synthetic seamount data extend
418 only 1.5 σ from the seamount center. This promotes better blending of the
419 synthetic seamounts into the regional bathymetry while retaining the data
420 having maximum slope which occur at 1.0 σ.

4) Create a 15-arcsecond grid following the methods in *Tozer et al.,* [2019].
5) Polish the step 4) grid with synthetic abyssal hills.
6) Polish the step 5) grid with synthetic seamounts.
7) Polish the step 6) grid with all the real soundings.
8) Combine the land topography data with the grid from 7).

Note this is a rather complex recipe. However, it is designed to inherit the long-wavelength shape of the ocean basins from original depth soundings. The satellite-derived gravity is used next to update the bathymetry in the 160-16 km wavelength band. Short wavelengths between 16 and 1 km are updated with synthetic abyssal hills. This is followed by an update using the Gaussian seamounts which, as in the real world, overprint the abyssal hills. Finally, the grid is polished using real depth soundings.

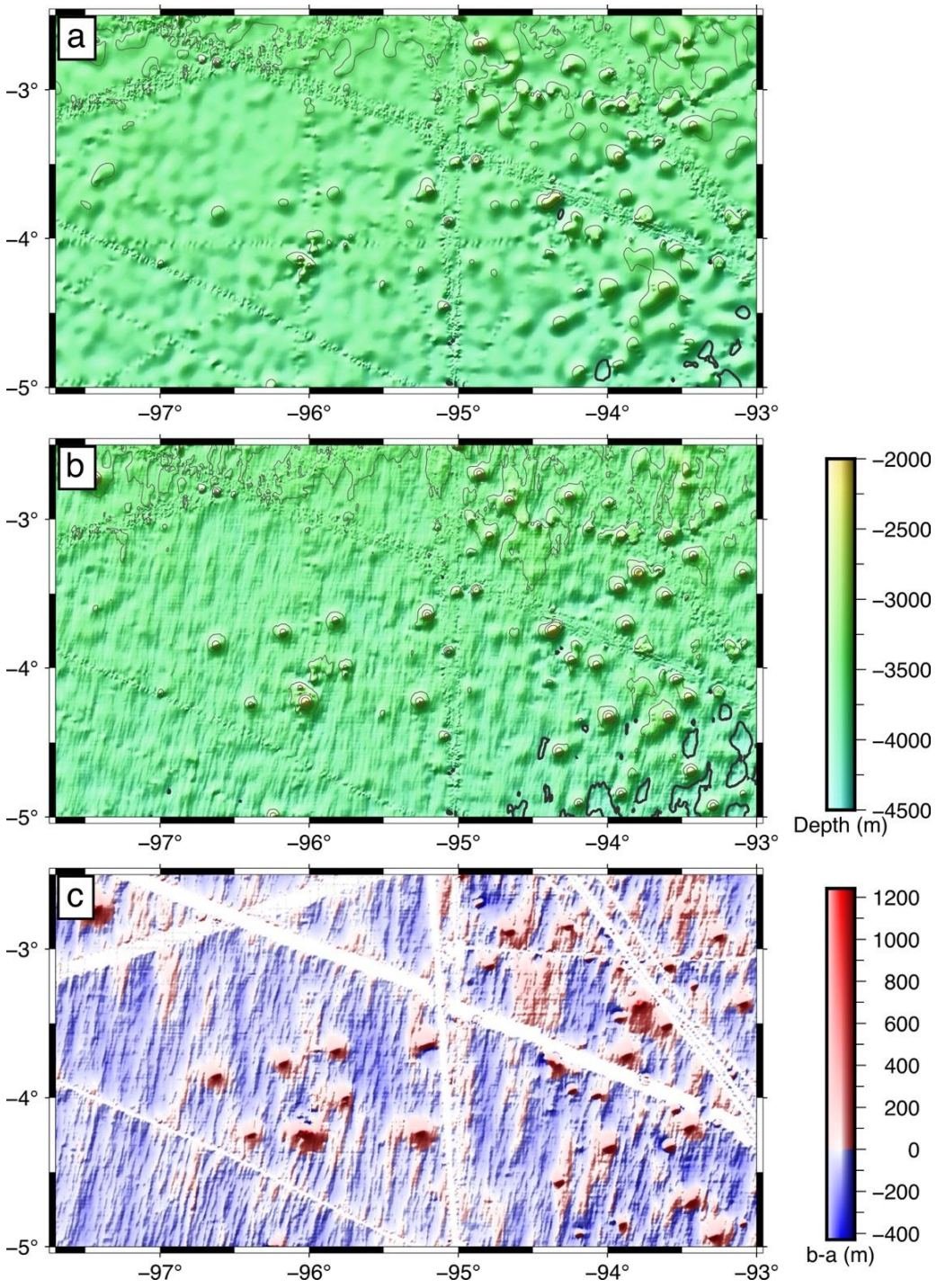

Figure 9. Bathymetry of an area south of the Galapagos spreading ridge. (a) Based on multi- and single-beam soundings and gravity-predicted bathymetry to fill the gaps. (b) Based on multi- and single-beam soundings, synthetic abyssal hills and sharpened seamounts superimposed on gravity-predicted bathymetry to fill the gaps. (c) Difference shows that the two methods are identical where measured soundings are available and have synthetic abyssal hills in other areas.

Uses of Synthetic bathymetry

This synthetic bathymetry has some appropriate uses as well as some uses that are inappropriate (Table 3) so it will be important to educate the users on how to use the product. A significant danger is that the general public could examine the synthetic bathymetry using a graphical tool such as Google Earth and conclude that the seafloor has been completely mapped at ~500 m resolution. Therefore, there must be an additional graphical layer, or style, to indicate what is real and what is synthetic.

The applications where this product is **not useful** are mainly aligned with GEBCO applications. These include seafloor geography and feature names. All of these synthetic features lie at base depths greater than ~1000 m so they are irrelevant for any kind of navigation except the 149 seamounts extending to within 200 m of the sea surface; these need to be flagged with red dots and eventually surveyed [https://www.star.nesdis.noaa.gov/star/documents/meetings/extReview/presentations/5CommTrans/CT2_WSmith.ppt]. This product is not useful for establishing the boundaries of the outer continental shelves for the law of the sea. The product is not useful for any kind of detailed deployment of seafloor instrumentation although it can provide a regional sense of seafloor roughness at scales larger than 1 km. The synthetic bathymetry is entirely confined to the deep ocean where sediments are thin so has no use for any applications on the continental margins.

There are three applications where this product is **marginally useful**. (1) In terms of education and outreach it could provide misinformation that we are done mapping the deep oceans. However, like the early hand-drawn bathymetric maps from *Heezen and Tharp* [1959] and GEBCO [*Hall,* 2006], the realistic synthetic bathymetry could inspire students to better understand marine geology and plate tectonics. (2) The product could help with establishing a range of possible tsunami propagation models based on

473 statistical realizations of abyssal fabric and seamounts [*Sepulveda et al.,* 2020]. (3) It
474 could be useful for understanding habitats over unmapped, moderately large
475 seamounts.
476
477 The synthetic bathymetry is **most useful** for studies where a realistic seafloor roughness
478 is needed. This includes models of ocean circulation [*Adcroft et al.,* 2004; *Chassignet et*
479 *al.,* 2007] and internal wave generation, dissipation, and mixing driven by tidal and other
480 low-frequency flows over the rough bottom [*Goff and Arbic*, 2010; *Polzin et al.,* 1997;
481 *Gille et al.,* 2000; *Jayne and St. Laurent,* 2001; *Egbert and Ray*, 2003]. In addition, rough
482 seafloor affects the propagation of acoustic waves [e.g., *Mckenzie,* 1961; *Chin-Bing et*
483 *al*.,1994]. The product could be useful for plate tectonic studies since one can see where
484 the abyssal hill fabric disagrees with nearby multibeam mapping which will provide data
485 on how to revise tectonic models. Finally, the product could be useful for planning
486 shipboard surveys of seamounts and volcanic ridges as well as a tool for planning the
487 optimal ship path for mapping rough seafloor.
488
489
490
491 Table 3. Appropriate applications of synthetic bathymetry

application	**yes**	**maybe**	**no**
seafloor geography and feature names			X
navigation			X
law of the sea			X
fiber optic cable route planning			X
coastal tide model improvements			X
education and outreach	X		X
tsunami propagation and hazard models		X	
fisheries management		X	
hydrodynamic tide models and tidal friction	X		
ocean circulation models	X		
tidal role in ocean mixing	X		

plate tectonics	X		
planning shipboard surveys	X		

Conclusions and Future Improvements

Our major conclusions are:

- Bathymetry predicted from satellite altimeter-derived gravity cannot resolve the small-scale fabric of the deep ocean associated with abyssal hills and seamounts. There are many remote areas that will not be mapped by ship in this decade.
- We extend two methods to fill these gaps with higher resolution synthetic bathymetry using information on the tectonics, geology, and sediment distribution in the deep oceans.
- Synthetic abyssal hills are generated using an anisotropic statistical model based on high resolution multibeam surveys in a variety of tectonic settings. The orientation of the hills uses the latest seafloor age maps.
- Small seamounts > 700 m tall can be accurately located in satellite-altimeter derived gravity but their shape cannot be resolved. We use ~800 well-surveyed small seamounts to calibrate the expected shapes of and create synthetic bathymetry for all seamounts in the 800-2500 m height range.
- These two synthetic data sets are used to add a small-scale bathymetry component (1-16 km) to the global predicted depth. This provides a new starting model for a remove/grid/restore re-gridding of available single and multibeam ship soundings.
- We generate two global bathymetry/topography products at 15 arcseconds using identical ship soundings. The SRTM15+ product has gaps filled with smooth predicted bathymetry and serves as the base layer for the 15 arcsecond GEBCO grid. The SYNBATH product has gaps filled with synthetic bathymetry from abyssal hills and seamounts superimposed on the smooth predicted bathymetry.
- The SRTM15+ product is suitable for applications in seafloor geography, law of the sea, seafloor instrumentation and cables and highlighting the need to fill the gaps before 2030.

- The SYNBATH product is suitable for any application where an accurate seafloor roughness is needed such as modeling ocean currents and tidal friction and the generation and dissipation of internal waves.

In the future we plan to continue to improve the resolution of gravity-predicted depth as well as to work with GEBCO to assemble more multibeam sounding data. With these efforts we can roll-back the spectral and spatial contributions of the synthetic bathymetry. Ka-band altimeters such as SARAL/AltiKa and SWOT promise a dramatic improvement in marine gravity/bathymetry accuracy and resolution.

Acknowledgements - This work was supported by the Office of Naval Research (N00014-17-1-2866), NASA SWOT program (NNX16AH64G and 80NSSC20K1138) and the Nippon Foundation through the SeaBed2030 project. The Generic Mapping Tools (GMT) [Wessel et al., 2019] were extensively used in data processing. The views, opinions, and findings contained in the report are those of the authors and should not be construed as an official National Oceanic and Atmospheric Administration or U.S. Government position, policy, or decision.

Open research and data availability - The global bathymetry grids, the global VGG grid, the characteristics of the 35,000 seamounts, and Google Earth overlays are all available at https://topex.ucsd.edu/pub/ . The VGG grids and overlays are in the global_grav_1min folder, the synthetic bathymetry and products are in the synbath folder, and the SRTM15+ bathymetry and products are in the srtm15_plus folder. Figures and most calculations were performed using GMT (https://www.generic-mapping-tools.org) and MATLAB (https://www.mathworks.com/products/matlab.html). Since 1994 we have stored previously published results in open archives at NGDC, NCEI, and Figshare. We also have all archived versions of our global grids in one location https://topex.ucsd.edu/pub/archive/ . We will be happy to use any data repository that the journal recommends.

References

Adcroft, A., Hill, C., Campin, J.M., Marshall, J. and Heimbach, P., 2004, September. Overview of the formulation and numerics of the MIT GCM. In Proceedings of the ECMWF seminar series on Numerical Methods, Recent developments in numerical methods for atmosphere and ocean modelling(pp. 139-149).

Becker, J.J. and Sandwell, D.T., 2008. Global estimates of seafloor slope from single-beam ship soundings. Journal of Geophysical Research: Oceans, 113(C5).

Caress, D.W. and Chayes, D.N., 2008. MB-System: Open source software for the processing and display of swath mapping sonar data. Internet: http://www. mbari. org/data/mbsystem.

Craig, C.H. and Sandwell, D.T., 1988. Global distribution of seamounts from Seasat profiles. Journal of Geophysical Research: Solid Earth, 93(B9), pp.10408-10420.

Chassignet, E.P., Hurlburt, H.E., Smedstad, O.M., Halliwell, G.R., Hogan, P.J., Wallcraft, A.J., Baraille, R. and Bleck, R., 2007. The HYCOM (hybrid coordinate ocean model) data assimilative system. *Journal of Marine Systems*, *65*(1-4), pp.60-83.

Chin-Bing, S.A., King, D.B., Murphy, J.E. and Li, G., 1994, July. Long-range cw and time-domain simulations of ocean acoustic scatter from Mid-Atlantic Ridge corners. In Automatic Object Recognition IV (Vol. 2234, pp. 188-194). International Society for Optics and Photonics.

Egbert, G.D. and Ray, R.D., 2003. Semi-diurnal and diurnal tidal dissipation from TOPEX/Poseidon altimetry. Geophysical Research Letters, 30(17).

Gevorgian, J., D. T. Sandwell, Y. Yu, S-S. Kim, P. Wessel, 2021, Global distribution and morphology of seamounts, T45D-0273, presented at Fall Meeting, AGU, New Orleans, LA, 13-17 December.

582 Gille, S.T., Yale, M.M. and Sandwell, D.T., 2000. Global correlation of mesoscale ocean variability
583 with seafloor roughness from satellite altimetry. Geophysical Research Letters, 27(9), pp.1251-
584 1254.
585
586 Goff, J.A. and Jordan, T.H., 1988. Stochastic modeling of seafloor morphology: Inversion of sea
587 beam data for second-order statistics. *Journal of Geophysical Research: Solid Earth*, *93*(B11),
588 pp.13589-13608.
589
590 Goff, J.A. and Jordan, T.H., 1989. Stochastic modeling of seafloor morphology: A parameterized
591 Gaussian model. Geophysical Research Letters, 16(1), pp.45-48.
592
593 Goff, J.A., 2020. Identifying characteristic and anomalous mantle from the complex relationship
594 between abyssal hill roughness and spreading rates. Geophysical Research Letters, 47(11),
595 p.e2020GL088162.
596
597 Goff, J.A. and Arbic, B.K., 2010. Global prediction of abyssal hill roughness statistics for use in
598 ocean models from digital maps of paleo-spreading rate, paleo-ridge orientation, and sediment
599 thickness. Ocean Modelling, 32(1-2), pp.36-43.
600
601 Hall, J.K., 2006. GEBCO Centennial Special Issue–Charting the secret world of the ocean floor:
602 the GEBCO project 1903–2003. Marine Geophysical Researches, 27(1), pp.1-5.
603
604 Hébert H., Deplus C., Huchon P., Khanbari K. et Audin L., 2001 - Lithospheric structure of a
605 nascent spreading ridge inferred from gravity data: the western Gulf of Aden - J. Geophys. Res.,
606 106 (B11), 26,345-26,363.
607
608 Heezen, B.C., Tharp, M. and Ewing, M., 1959. The floors of the oceans: I. The North Atlantic (Vol.
609 65). Geological Society of America.
610
611 Jayne, S.R. and St. Laurent, L.C., 2001. Parameterizing tidal dissipation over rough topography.
612 Geophysical Research Letters, 28(5), pp.811-814.
613

614 Kim S. and Wessel., 2011. New global seamount census from altimetry-derived gravity data.
615 Geophysical Journal International. vol. 186, p. 615-631
616
617
618 Kim, S.S. and Wessel, P., 2015, October. Finding seamounts with altimetry-derived gravity data.
619 In OCEANS 2015-MTS/IEEE Washington (pp. 1-6). IEEE.
620
621 Loubrieu Benoît. Bathymetry - Kerguelen Islands (synthesis, 2019) cell size 200 m. Ifremer
622 http://dx.doi.org/10.12770/1909f2fb-09ee-49e3-8b5f-52b12e53d292
623
624 Loubrieu Benoît. Bathymetry of the French Guiana margin and Demerara Plateau / Data
625 compilation 2019. Ifremer http://dx.doi.org/10.12770/1f127956-8350-466e-b795-
626 c8a9eb3c218e
627
628 Loubrieu Benoît, Royer Jean-Yves, Maia Marcia (2020). Bathymetry around Saint-Paul and
629 Amsterdam Islands / Data compilation 2020. Ifremer http://dx.doi.org/10.12770/342b2892-
630 b0de-4566-bd77-520fb3bf4eaa
631
632 Mackenzie, K.V., 1961. Bottom Reverberation for 530-and 1030-cps Sound in Deep Water. The
633 journal of the acoustical society of America, 33(11), pp.1498-1504.
634
635 Matthews, K.J., Müller, R.D., Wessel, P. and Whittaker, J.M., 2011. The tectonic fabric of the
636 ocean basins. Journal of Geophysical Research: Solid Earth, 116(B12).
637
638 Mayer, L., Jakobsson, M., Allen, G., Dorschel, B., Falconer, R., Ferrini, V., Lamarche, G., Snaith, H.
639 and Weatherall, P., 2018. The Nippon Foundation—GEBCO seabed 2030 project: The quest to
640 see the world's oceans completely mapped by 2030. Geosciences, 8(2), p.63.
641
642 Menard H. W., 1964. Marine Geology of the Pacific. McGraw Hill, New York
643
644 Mendel V., Sauter D., Patriat P. and Munschy M., 2000. Relationship of the Central Indian Ridge
645 segmentation with the evolution of the Rodrigues triple junction for the past 8 Ma. J. Geophys.
646 Res, 105, 16563-16576

Parker, R.L., 1973. The rapid calculation of potential anomalies. Geophysical Journal International, 31(4), pp.447-455.

Polzin, K.L., Toole, J.M., Ledwell, J.R. and Schmitt, R.W., 1997. Spatial variability of turbulent mixing in the abyssal ocean. Science, 276(5309), pp.93-96.

Ruellan, Etienne. North Fiji Basin (Southwest Pacific) - 1000m. Ifremer https://doi.org/10.12770/f651de98-9478-4d42-9dc9-c0ec7a43ae87

Sandwell, D.T. and Smith, W.H., 2009. Global marine gravity from retracked Geosat and ERS-1 altimetry: Ridge segmentation versus spreading rate. Journal of Geophysical Research: Solid Earth, 114(B1).

Sandwell, D.T., Müller, R.D., Smith, W.H., Garcia, E. and Francis, R., 2014. New global marine gravity model from CryoSat-2 and Jason-1 reveals buried tectonic structure. Science, 346(6205), pp.65-67.

Sandwell, D.T., Harper, H., Tozer, B. and Smith, W.H., 2019. Gravity field recovery from geodetic altimeter missions. Advances in Space Research.

Sauter, D. and V. Mendel. The southwest indian ridge between 65°E and 68°E - 120m. Ifremer https://doi.org/10.12770/e54561cf-a7aa-4336-a935-7cfec6e1cdbb

Seton, M., Müller, R.D., Zahirovic, S., Williams, S., Wright, N.M., Cannon, J., Whittaker, J.M., Matthews, K.J. and McGirr, R., 2020. A Global Data Set of Present-Day Oceanic Crustal Age and Seafloor Spreading Parameters. Geochemistry, Geophysics, Geosystems, 21(10), p.e2020GC009214.

Smith D., 1988. Shape Analysis of Pacific Seamounts. Earth and Planetary Science Letters, vol. 90. p.457-466

680 Smith D. and Jordan T., 1988. Seamount Statistics in the Pacific Ocean. Journal of Geophysical
681 Research, vol. 94, No. B4, p. 2899-2918
682
683 Sepúlveda, I., Tozer, B., Haase, J.S., Liu, P.L.F. and Grigoriu, M., 2020. Modeling uncertainties of
684 bathymetry predicted with satellite altimetry data and application to tsunami hazard
685 assessments. Journal of Geophysical Research: Solid Earth, 125(9), p.e2020JB019735.
686
687 Sisavath, E., Babonneau, N., Saint-Ange, F., Bachèlery, P., Jorry, S.J., Deplus, C., De Voogd, B. and
688 Savoye, B., 2011. Morphology and sedimentary architecture of a modern volcaniclastic turbidite
689 system: The Cilaos fan, offshore La Réunion Island. Marine Geology, 288(1-4), pp.1-17.
690
691 Smith, W.H. and Sandwell, D.T., 1994. Bathymetric prediction from dense satellite altimetry and
692 sparse shipboard bathymetry. Journal of Geophysical Research: Solid Earth, 99(B11), pp.21803-
693 21824.
694
695 Smith, W.H.F. and Wessel, P., 1990. Gridding with continuous curvature splines in tension.
696 Geophysics, 55(3), pp.293-305.
697
698 Staudigel H, Koppers A, Lavelle W, et al., 2010. Defining the Word “Seamount”. Oceanography,
699 vol. 23, No 1, p. 20-21.
700
701 Straume, E.O., Gaina, C., Medvedev, S., Hochmuth, K., Gohl, K., Whittaker, J.M., Abdul Fattah, R.,
702 Doornenbal, J.C. and Hopper, J.R., 2019. GlobSed: Updated total sediment thickness in the
703 world's oceans. Geochemistry, Geophysics, Geosystems, 20(4), pp.1756-1772.
704
705 Talbot, S. and B. Loubrieu, https://w3.ifremer.fr/archimer/doc/00613/72480/
706 https://sextant.ifremer.fr/eng/Data/Catalogue#/metadata/915d04a1-220f-4784-934c-
707 c269a515e5a9
708
709 Tozer, B., Sandwell, D.T., Smith, W.H., Olson, C., Beale, J.R. and Wessel, P., 2019. Global
710 bathymetry and topography at 15 arc sec: SRTM15+. Earth and Space Science, 6(10), pp.1847-
711 1864.
712

713 Yesson, C., Clark, M.R., Taylor, M.L. and Rogers, A.D., 2011. The global distribution of seamounts
714 based on 30 arc seconds bathymetry data. Deep Sea Research Part I: Oceanographic Research
715 Papers, 58(4), pp.442-453.
716
717 Watts, A. B., Sandwell, D. T., Smith, W. H. F., & Wessel, P. (2006). Global gravity, bathymetry,
718 and the distribution of submarine volcanism through space and time. Journal of Geophysical
719 Research, 111(B8). https://doi.org/10.1029/2005JB004083
720
721 Weatherall et al., GEBCO Bathymetric Compilation Group 2020 (2020). The GEBCO_2020 Grid - a
722 continuous terrain model of the global oceans and land. British Oceanographic Data Centre,
723 National Oceanography Centre, NERC, UK. doi:10/dtg3.
724
725 Wessel, P., 2001. Global distribution of seamounts inferred from gridded Geosat/ERS-1
726 altimetry. Journal of Geophysical Research: Solid Earth, 106(B9), pp.19431-19441.
727
728 Wessel, P., Luis, J.F., Uieda, L., Scharroo, R., Wobbe, F., Smith, W.H.F. and Tian, D., 2019. The
729 generic mapping tools version 6. Geochemistry, Geophysics, Geosystems, 20(11), pp.5556-5564.
730
731 Wessel P., 1997. Sizes and Ages of Seamounts Using Remote Sensing: Implications for Intraplate
732 Volcanism. Science, vol. 277, p. 802-805
733
734 Wessel, P., Luis, J. F., Uieda, L., Scharroo, R., Wobbe, F., Smith, W. H. F., & Tian, D. (2019). The
735 Generic Mapping Tools version 6. Geochemistry, Geophysics, Geosystems, 20, 5556–5564.
736 https://doi.org/10.1029/2019GC008515
737
738 Wessel P, Sandwell D, and Kim S., 2010. The Global Seamount Census. Special Issue on
739 Mountains in the Sea, Oceanography, vol. 23, No. 1, p. 24-33
740